

A census of orbital properties of the M31 satellites

Laura L. Watkins^{1,2*}, N. Wyn Evans², Glenn van de Ven¹

¹Max Planck Institute for Astronomy, Königstuhl 17, Heidelberg 69117, Germany

²Institute of Astronomy, University of Cambridge, Madingley Road, Cambridge, CB3 0HA, UK

Accepted ???; Received ???; Submitted ???

ABSTRACT

We present an analysis of the dynamics of the M31 satellite system. Proper motion data exist for only two of the M31 satellites. We account for this incompleteness in velocity data by a statistical analysis using a combination of the timing argument and phase-space distribution functions. The bulk of the M31 satellites are well fit by these models and we offer a table of orbital properties, including period, eccentricity and semi-major axis. This enables us to search for evidence of group infall based on orbital similarity rather than propinquity on the sky. Our results favour an association between Cass II and NGC 185, as the orbital parameters are in close agreement, but not for NGC 185 and NGC 147, which have often been associated in the past. Other possible satellite groupings include the pair And I and And XVII; the pair And IX and And X; and the triple And V, And XXV and NGC 147. And XXII has been claimed as a satellite of M33; we find that they are not moving independently along the same orbit, but cannot determine whether they are orbiting each other or are unrelated. Two satellites, And XII and And XIV, have high line-of-sight velocities, consistent with very recent infall from the edge of the Local Group. They are not well described by our underlying smooth phase space distribution function, and are reanalysed without priors on their orbital parameters. For And XIV, multiple pericentric passages are possible and improved distance information is needed to draw further conclusions. For And XII, orbits which assume at least one pericentric passage can be ruled out and it must be on its first infall into the M31 system.

Key words: galaxies:individual: M31 – galaxies: dwarf – galaxies: kinematics and dynamics – Local Group

1 INTRODUCTION

In this paper, we present an analysis of the distances and velocities of the satellites of M31 within the framework of the timing argument. There have been a number of wide field surveys of M31 in recent years that have more than doubled the number of satellites (Zucker et al. 2004, 2007; Martin et al. 2006; Majewski et al. 2007; Ibata et al. 2007; Irwin et al. 2008; McConnachie et al. 2008; Martin et al. 2009; Richardson et al. 2011; Slater et al. 2011; Bell et al. 2011; Irwin et al. 2012). Spectroscopic follow-up has provided radial velocities for almost all the new discoveries (e.g. Tollerud et al. 2012; Collins et al. 2012) and the existing dataset is now substantial. However, proper motion data are not currently measurable with existing optical telescopes. For only two of the M31 satellites (M33 and IC 10) can proper motions be derived using VLBI observations of maser emission from star-forming regions. Although future, deeper surveys will discover many more such galaxies (e.g., SkyMapper, LSST), now seems an opportune moment to analyse the orbital properties of the known satellites.

The M31 galaxy is believed to have had a more violent accretion history than the Milky Way. Its stellar halo is more dense

and extended than that of the Milky Way, its collection of satellite galaxies and globular clusters more numerous. Two of the entourage, And XII (Martin et al. 2006; Chapman et al. 2007; Collins et al. 2010) and And XIV (Majewski et al. 2007; Kalirai et al. 2010), are unusual in that they have extreme kinematics with high line-of-sight velocities. And XII may have been formed outside of the virial radius of the Local Group (Chapman et al. 2007) and only recently been accreted. Similarly, Majewski et al. (2007) found that, even at its projected radius, And XIV is nearly at the M31 escape velocity, which implies that And XIV may also be on its first infall into the Local Group. Hierarchical models of formation can often produce dSphs on eccentric orbits at late times, as the smaller galaxies begin to interact with the nascent, central galaxy. For example, Sales et al. (2007) suggested that infall of a satellite pair, followed by a three-body encounter may detach the lighter companion and eject it on to an eccentric orbit. Such satellites may be identifiable as outliers in a census of orbital properties.

The main hurdle is that, for most of the M31 satellites, only the line-of-sight velocities are known; there are no proper motions. This means that statistical techniques have to be developed to associate characteristic orbital periods, eccentricities, semi-major axes and numbers of pericentric passages with each satellite galaxy. We show how to do this with a novel combination of the timing argu-

* watkins@mpia.de

ment and phase-space distribution functions. The principle behind the timing argument is simple: for two galaxies that are nearby and moving towards each other at the present time, we assume that, at the time of the Big Bang, they were close together and began to move apart with the Hubble expansion. At high redshift, their mutual gravitational attraction would have caused them to decouple from the Hubble flow and their orbit can then be described using Newtonian dynamics. Given their present separation and velocities and the time for which they have been interacting, we can estimate the properties of their orbit.

Kahn & Woltjer (1959) first applied the timing argument to the relative motion of the Milky Way and M31 to infer that there must be a significant amount of intergalactic mass in the Local Group. This analysis has been re-visited in the intervening years (e.g. van der Marel & Guhathakurta 2008) and, more recently, it has been applied to certain of the Milky Way satellites in order to estimate the Milky Way mass (Li & White 2008; Kallivayalil et al. 2009). Of course, the timing argument treats the two galaxies as point masses, which is clearly an oversimplification. Galaxies are extended objects, and have themselves evolved and accreted a significant amount of mass since the Big Bang. Li & White (2008) studied analogues of the Local Group in the Millennium Simulation to show that the timing argument gives an almost unbiased estimate of the combined mass of two large galaxies, like the Milky Way and M31. They then extended the analysis to a large galaxy with a smaller satellite and showed that it is equally effective for determining the host mass. So it seems that, despite the rather generous assumptions, the timing argument is surprisingly effective.

Section 2 introduces the data for the M31 satellites. Section 3 introduces a distribution of semi-major axes and eccentricities for a satellite galaxy population in the outer parts of M31, and shows how to fix the parameters via a maximum likelihood method. Section 4 implements the algorithm, and provides maximum likelihood solutions for the whole dataset, as well as individual satellites. For each satellite, we provide the most likely orbital period, eccentricity, semi-major axis in Table 2. In Section 5, we identify possible candidates for group infall. Section 6 relaxes some of the assumptions we make earlier in the paper and reanalyses a number of satellites that are not well fit by the earlier models; seeking minimum mass solutions to the Timing Argument to account for the lack of proper motion data. Finally, we conclude in Section 7.

2 DATA

The position and velocity data for M31 and its satellites are given in Table 1. The locations of the satellites are shown in Fig. 1 in equatorial coordinates, with the position of M31 shown as an ellipse (the size of which corresponds to the extent of the disk). The points are coloured according to the orbital periods that we derive in Section 4.4. The shaded region shows the PAndAS footprint to illustrate the bias in the spatial coverage of current deep surveys.

Distance estimates for most of the galaxies are from the profiles presented by Conn et al. (2012); although we quote distances and errors in the table, we do not use these directly in the first part of our analysis, instead we use the full heliocentric distance profiles. Where distance profiles are not available, we assume the profiles are Gaussian.

The majority of the dSph velocities come from Tollerud et al. (2012) and Collins et al. (2012). If a satellite has been studied by both groups, we follow the advice of Collins et al. (2012) and use the estimate based on a greater number of member stars. There are

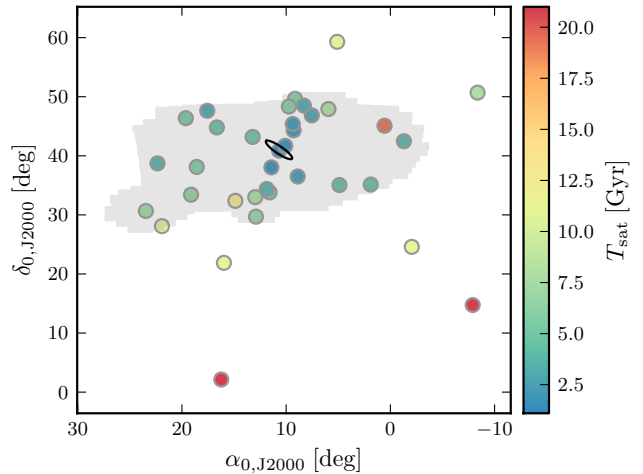


Figure 1. Positions of the satellites in equatorial coordinates; the points are coloured according to the estimated period of the satellite’s orbit (see Section 4.4 for details and Table 2 for full satellite orbital properties). The ellipse shows the extent of the bright disk of M31. The PAndAS footprint is shaded to illustrate the bias in the spatial coverage of current deep surveys.

some instances in which the heliocentric velocities have asymmetric errors; as these are generally only different by small amounts, we adopt the mean of the error.

We use the M31 proper motions $(\mu_\alpha, \mu_\delta) = (34.3 \pm 8.6, -20.2 \pm 7.8) \mu\text{as yr}^{-1}$ recently presented in van der Marel et al. (2012); that study assumed a fixed M31 distance, whereas here we consider the full posterior distance distribution (Conn et al. 2012). This makes it necessary to adjust the proper motions to account for this change.

3 MONTE CARLO SIMULATIONS

With proper motions as well as line-of-sight velocities for all of the M31 satellites, we could determine both the radial and tangential components of the satellite motions. Unfortunately, proper motion data exist for only two of the satellites: IC 10 and M33; for the rest, there are only line-of-sight velocities. If we wish to gain insights into the properties of the orbits, we must turn to a more statistical analysis.

To start, we generate a population of N_{orb} satellites around a central host, with their orbits described by the timing argument. We then view each of the satellites from N_{pos} randomly selected viewing positions in order to determine line-of-sight velocities. Finally, we determine how likely each M31 satellite is in a given model.

3.1 The timing argument

To apply the timing argument to M31 and any one of its satellites, we solve the following set of equations for spherical radius r from the centre of M31, time t , radial velocity v_r and tangential velocity v_t of the satellite:

$$\begin{aligned} r &= a(1 - e \cos \eta), & t &= \frac{a}{\lambda} (\eta - e \sin \eta), \\ v_r &= \lambda \frac{e \sin \eta}{1 - e \cos \eta}, & v_t &= \lambda \frac{\sqrt{1 - e^2}}{1 - e \cos \eta}, \end{aligned} \quad (1)$$

where η is the eccentric anomaly, e is the eccentricity of the orbit, a is the semi-major axis of the orbit, M is the total mass of the system

Table 1. Data table for the Local Group galaxies used in this analysis.

	$\alpha_{0,J2000}$	$\delta_{0,J2000}$	d_h (kpc)	v_h (km/s)	sources ^a
M31	00 42 44.3	+41 16 09.0	779 ⁺¹⁹ ₋₁₈	-301.0 ± 1.0	1,2,3
And I	00 45 39.8	+38 02 28.0	727 ⁺¹⁸ ₋₁₇	-376.3 ± 2.2	1,2,14
And II	01 16 29.8	+33 25 09.0	630 ± 15	-193.6 ± 1.0	1,2,14
And III	00 35 33.8	+36 29 52.0	723 ⁺¹⁸ ₋₂₄	-344.3 ± 1.7	1,2,14
And V	01 10 17.1	+47 37 41.0	742 ⁺²¹ ₋₂₂	-397.3 ± 1.5	1,2,15
And VI (Peg dSph)	23 51 46.3	+24 34 57.0	783 ± 25	-340.8 ± 1.9	1,1,14
And VII (Cass I)	23 26 31.0	+50 41 31.0	763 ± 35	-307.2 ± 1.3	1,1,14
And IX	00 52 51.1	+43 11 48.6	600 ⁺⁹¹ ₋₂₃	-209.4 ± 2.5	4,2,15
And X	01 06 35.3	+44 48 03.8	670 ⁺²⁴ ₋₃₉	-164.1 ± 1.7	5,2,14
And XI	00 46 21.0	+33 48 22.0	763 ⁺²⁹ ₋₁₀₆	-427.0 ^{+2.9} _{-2.8}	4,2,14
And XII	00 47 27.0	+34 22 29.0	928 ⁺⁴⁰ ₋₁₃₆	-557.1 ± 1.7	4,2,14
And XIII	00 51 51.0	+33 00 16.0	760 ⁺¹²⁶ ₋₁₅₄	-185.4 ± 2.4	4,2,15
And XIV	00 51 35.0	+29 41 49.0	793 ⁺²³ ₋₁₇₉	-480.6 ± 1.2	4,2,14
And XV	01 14 18.7	+38 07 03.0	626 ⁺⁷⁹ ₋₃₅	-323.0 ± 1.4	4,2,15
And XVI	00 59 29.8	+32 22 36.0	476 ⁺⁴⁴ ₋₂₉	-367.3 ± 2.8	4,2,15
And XVII	00 37 08.0	+44 18 53.0	727 ⁺³⁹ ₋₂₅	-251.1 ^{+1.5} _{-1.6}	5,2,14
And XVIII	00 02 14.5	+45 05 20.0	1214 ⁺⁴⁰ ₋₄₃	-332.1 ± 2.7	6,2,15
And XIX	00 19 32.1	+35 02 37.1	821 ⁺³² ₋₁₄₈	-111.2 ^{+1.2} _{-1.3}	6,2,14
And XX	00 07 30.7	+35 07 56.4	741 ⁺⁴² ₋₅₂	-456.2 ^{+3.0} _{-3.4}	6,2,14
And XXI	23 54 47.7	+42 28 15.0	827 ⁺²³ ₋₂₅	-362.7 ± 0.8	7,2,14
And XXII (Tri I)	01 27 40.0	+28 05 25.0	920 ⁺³² ₋₁₃₉	-129.0 ^{+2.1} _{-2.2}	7,2,15
And XXIII	01 29 21.8	+38 43 08.0	748 ⁺³¹ ₋₂₁	-242.7 ± 1.0	8,2,14
And XXIV	01 18 30.0	+46 21 58.0	898 ⁺²⁸ ₋₄₂	-127.8 ^{+5.3} _{-5.4}	8,2,14
And XXV	00 30 08.9	+46 51 07.0	736 ⁺²³ ₋₆₉	-107.8 ^{+1.0} _{-0.9}	8,2,14
And XXVI	00 23 45.6	+47 54 58.0	754 ⁺²¹⁸ ₋₁₆₄	-260.6 ^{+4.0} _{-3.7}	8,2,14
And XXVII	00 37 27.1	+45 23 13.0	1255 ⁺⁴² ₋₄₇₄	-534.8 ^{+5.4} _{-4.9}	8,2,14
Cass II (And XXX)	00 36 34.9	+49 38 48.0	681 ⁺³² ₋₇₈	-141.4 ^{+5.8} _{-6.7}	9,2,14
IC 10	00 20 24.5	+59 17 30.0	660 ± 66	-348.0 ± 1.0	10,11,16
IC 1613	01 04 54.1	+02 07 60.0	715 ± 40	-232.0 ± 1.0	10,12,16
M32	00 42 42.1	+40 51 59.0	781 ± 20	-200.0 ± 6.0	10,13,16
M33	01 33 50.9	+30 39 36.0	820 ⁺²⁰ ₋₁₉	-180.0 ± 1.0	1,2,16
NGC 147	00 33 12.1	+48 30 32.0	712 ⁺²¹ ₋₁₉	-193.0 ± 3.0	1,2,17
NGC 185	00 38 58.0	+48 20 15.0	620 ⁺¹⁹ ₋₁₈	-202.0 ± 3.0	1,2,17
NGC 205	00 40 22.1	+41 41 07.0	824 ± 27	-241.0 ± 3.0	1,1,17
Pegasus	23 28 23.2	+14 44 35.0	919 ± 30	-184.5 ± 0.3	1,1,18
Pisces	01 03 52.9	+21 53 05.0	769 ± 23	-286.5 ± 0.3	1,1,18

Notes: ^a sources are given in turn for position, distance, line-of-sight velocity

Sources: (1) McConnachie et al. (2005); (2) Conn et al. (2012); (3) Courteau & van den Bergh (1999); (4) Collins et al. (2010); (5) Brasseur et al. (2011); (6) McConnachie et al. (2008); (7) Martin et al. (2009); (8) Richardson et al. (2011); (9) Irwin et al. (2012); (10) Karachentsev et al. (2004); (11) Sakai et al. (1999); (12) Cole et al. (1999); (13) see Appendix A; (14) Collins et al. (2012); (15) Tollerud et al. (2012); (16) Huchra et al. (1999); (17) Bender et al. (1991); (18) Huchtmeier et al. (2003)

and $\lambda = (GM/a)^{\frac{1}{2}}$. For each host-satellite pair, we assume that their mutual gravitational attraction caused them to decouple from the Hubble flow at high redshift. Thus, the time t is the age of the universe, which is $t_u = 13.73_{-0.15}^{+0.16}$ Gyr (Spergel et al. 2007).

3.2 Models

In the nearly-Keplerian regime in which the Galactic potential is $\phi \propto r^{-\beta}$ with $\beta \approx 1$, a density distribution that falls like $\rho \propto r^{-\gamma}$ is generated by a phase space distribution function (Evans et al. 1997)

$$f(E, L) \propto |L|^{2m} |E|^\alpha, \quad \alpha = \frac{(2 - \beta)m + \gamma}{\beta} - \frac{3}{2} \quad (2)$$

or equivalently

$$f(a, e) \propto (1 - e^2)^m a^{m-\alpha}. \quad (3)$$

The distributions of semi-major axes a and eccentricities e are given by

$$f(a) \propto a^{\frac{3}{2}-\gamma}, \quad f(e) \propto (1 - e^2)^m. \quad (4)$$

Note that γ alone controls the distribution of semi-major axes whilst m controls the distribution of eccentricities. The shapes of these distributions are shown in Fig. 2; the solid lines represent the functional form of the distributions, the histograms show samples selected at random from the given distributions. The left panel shows the semi-major axis distributions for various γ ; for $\gamma = 1$, the distribution of semi-major axes is nearly flat, with a slight preference for large values of a , but as γ increases the distributions strongly favour smaller semi-major axes and the distributions are highly peaked. The right panel shows the eccentricity distributions

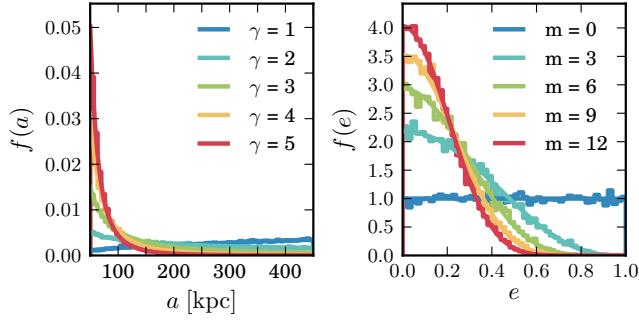


Figure 2. Left panel: the distribution of semi-major axes for different values of γ . Right panel: the distribution of orbital eccentricities for different values of m . In both panels, the smooth lines represent the analytical distributions (see equation (4)) and the histograms represent samples of selected at random from the given distribution.

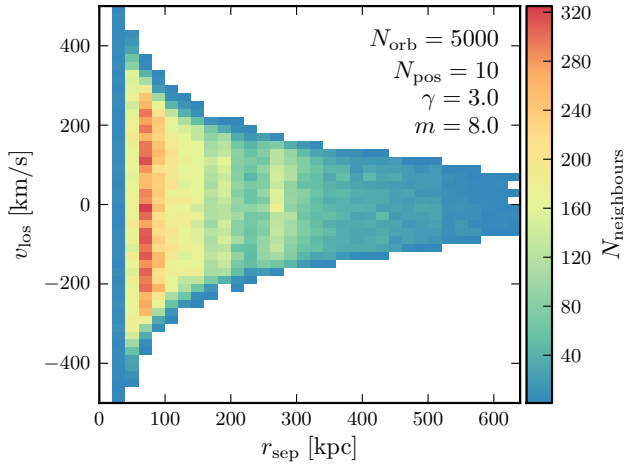


Figure 3. The distribution of host-satellite separations and absolute line-of-sight velocities for a model with $\gamma = 3.0$, $m = 8.0$, $N_{\text{orb}} = 5000$ and $N_{\text{pos}} = 10$. The points are binned into pixels of size $20 \text{ kpc} \times 20 \text{ km s}^{-1}$ and the pixels coloured according to the number of points therein. For clarity, the v_{los} axis has been truncated at $\pm 500 \text{ km s}^{-1}$.

for a range of m . For $m = 0$, the distribution of eccentricities is flat; as m increases, the distributions begin to favour low eccentricities, until for high m the most eccentric orbits are effectively ruled out.

For given γ and m , we generate N_{orb} (a, e) pairs from these distributions. We adopt an M31 mass of $M_{\text{M31}} = 1.5 \times 10^{12} M_{\odot}$ (Watkins et al. 2010) and assume a universal satellite mass of $M_{\text{sat}} = 1 \times 10^7 M_{\odot}$ (e.g. Strigari et al. 2008); then the total system mass $M = M_{\text{M31}} + M_{\text{sat}}$. Now we use equation (1) to propagate the orbits forwards until $t = t_{\text{u}}$ (with corresponding eccentric anomaly $\eta = \eta_{\text{u}}$). The values of r at this point are the host-satellite separations.

To fix the viewing positions, we select a host-observer distance d from the heliocentric distance profile of M31 (Conn et al. 2012). We generate position angles (l, b) , where l is selected at random in $[0, 2\pi]$ and $\sin b$ is selected at random in $[0, 1]$. N_{pos} viewing positions are generated separately for each of the N_{orb} orbits. For each viewing position, the component of the satellite's velocity v_{los} along the line-of-sight is calculated.

Now we have a set of $N = N_{\text{orb}} \times N_{\text{pos}}$ simulated satellites, each with a host-satellite separation distance r and a line-of-sight velocity v_{los} . A sample distribution of separation distances and line-of-sight velocities is shown in Fig. 3, generated with parameters: $\gamma = 3.0$, $m = 8.0$, $N_{\text{orb}} = 5000$ and $N_{\text{pos}} = 10$ (see Section 4.1 for a discussion of how N_{orb} and N_{pos} are chosen). As a visual aid, to highlight the density of the points, the points have been binned into $10 \text{ kpc} \times 10 \text{ km s}^{-1}$ pixels and the pixels coloured according to the number of points they contain.

3.3 Satellite likelihoods

For a given model, we wish to determine how likely it is that we observe a particular satellite given the model predictions, and also, how likely it is that we observe the whole satellite system.

For each satellite, we have data Θ_{sat} that consists of the sky coordinates of the satellite (for which we assume no errors), the heliocentric distance of the satellite and errors, the observed radial velocity of the satellite and error, and (where available) the proper motions of the satellite and errors; together with the same data for M31. We assume the error distributions are Gaussian, although for the satellite distances, we allow the positive error to be different from the negative error.

From this data, we can calculate the distributions of separations r of the satellite from the centre of M31 and the line-of-sight velocities v_{los} of the satellite corrected for solar peculiar motion¹, motion of the Local Standard of Rest (LSR)² and the relative motion of the Milky Way and M31. In what follows, for greater clarity, we will drop the LOS subscript on v_{los} , but we will always be considering line-of-sight velocities.

We start by generating 10^5 sets of data Θ_{sat} from their respective distributions, and calculate r and v for each set. As expected, the distribution of velocities is approximately Gaussian, with a mean v_{sat} similar to that calculated using the data values and a standard deviation $\sigma_{v_{\text{sat}}}$ comparable to that inferred from standard error propagation. The distribution of separations requires some further thought. The separation distance r is calculated via,

$$r^2 = d^2 + d_{\text{M31}}^2 - 2dd_{\text{M31}} \cos \theta, \quad (5)$$

where d is the heliocentric distance of the satellite, d_{M31} is the heliocentric distance of M31 and θ is their angular separation. There is a minimum separation distance $r_{\text{min}} = d_{\text{M31}} \sin \theta$ (achieved when $d = d_{\text{M31}} \cos \theta$). Even when the satellite heliocentric distances are normally distributed, the resulting separation distribution cannot be obtained by simply truncating the Gaussian at r_{min} and renormalising because the distribution can become significantly non-Gaussian. The distribution accumulates near the minimum because of the complicated dependence of the separation distance on the satellite position. When the satellite distance profiles are non-Gaussian (as they are for many satellites in this analysis, see Conn et al. 2012), the separation distributions become yet more complex.

Fig. 4 shows the distribution of separations for three typical satellites. Satellites such as And II are either far enough away from the centre of M31 or have small enough errors that the minimum separation is never reached and the distribution does not pile up at small separations. For satellites such as And XX, the distributions

¹ $(U_0, V_0, W_0) = (10.00 \pm 0.36, 5.25 \pm 0.62, 7.17 \pm 0.38) \text{ km s}^{-1}$ (Dehnen & Binney 1998).

² $V_{\text{LSR}} = 220 \pm 20 \text{ km s}^{-1}$ (Kerr & Lynden-Bell 1986).

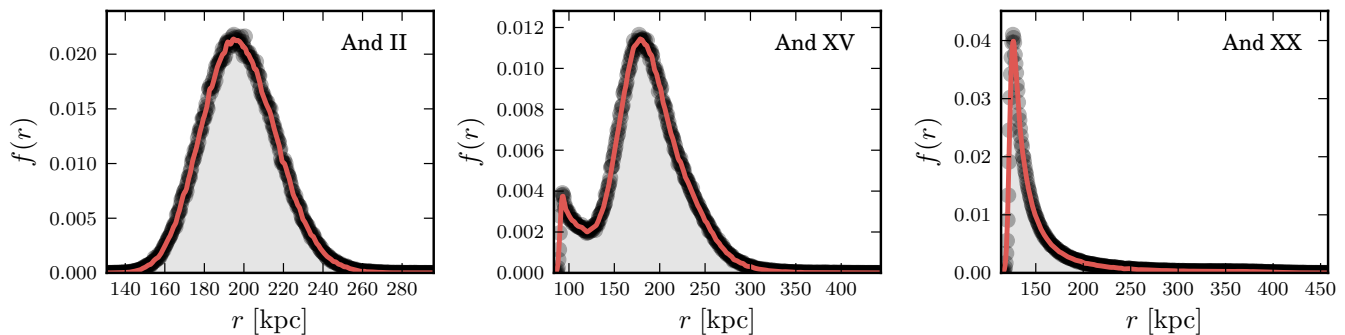


Figure 4. The distribution of separations for And II (left), And XV (middle) and And XX (right). And II is sufficiently distant with small enough errors so that the shape of the separation profile is similar to that of the heliocentric distance profile. And XV is an intermediate case, as its separation distribution is similar to the heliocentric distance distribution at larger separations, but this breaks down close to the minimum separation. For And XX, the distribution finds a minimum separation distance around which the distribution becomes highly peaked. The red lines show the functions fitted to the distributions.

are highly distorted with a sharp peak at or near the minimum separation distance. The final example, And XV, is an intermediate case that is just starting to show an increase in separations near the minimum separation distance. In order to account for these profiles in our models, we approximate the functional forms of the likelihood distributions by fitting splines to the smoothed histograms. These functions $f(r)$ are shown by the red lines in Fig. 4. We include the full set of separation-distance distributions in Fig. B1.

For each model, we have a set of N pairs of separation distances and line-of-sight velocities $\{\Theta_i = (r_i, v_i)\}_{i=1}^N$. For each point, we ask what is the likelihood of observing Θ_{sat} ,

$$\begin{aligned} P(\Theta_{\text{sat}}|\Theta_i, \gamma, m) &= CP(\Theta_{\text{sat}}|r_i, \gamma, m)P(\Theta_{\text{sat}}|v_i, \gamma, m) \\ &= Cf(r_i) \exp\left(-\frac{(v_i - v_{\text{sat}})^2}{2\sigma_{v_{\text{sat}}}^2}\right), \end{aligned} \quad (6)$$

for normalising constant C . The likelihood of observing the satellite given the model is then the weighted sum over all points Θ_i ,

$$P(\Theta_{\text{sat}}|\gamma, m) = \sum_{i=1}^N P(\Theta_{\text{sat}}|\Theta_i, \gamma, m) P(\Theta_i). \quad (7)$$

The weights $P(\Theta_i) = 1/N$ in this case, as the priors on Θ_i are already accounted for in the Monte Carlo modelling.

The likelihood of observing the whole satellite system Θ_{sys} , is the product of the individual likelihoods for each satellite and is thus

$$P(\Theta_{\text{sys}}|\gamma, m) = \prod_{\text{satellites}} P(\Theta_{\text{sat}}|\gamma, m). \quad (8)$$

4 RESULTS

4.1 Setup

Recall, we wish to sample N_{orb} orbits from the distributions given in equation (4), and to “observe” each orbit from N_{pos} viewing positions. The total number of points $N_{\text{tot}} = N_{\text{orb}} \times N_{\text{pos}}$ should be as large as possible to ensure that the rv -space is well sampled. We find that $N_{\text{tot}} = 10^6$ is sufficient for this purpose. N_{orb} controls the number of radii sampled, while N_{pos} is the number of velocities sampled at each radius. Provided N_{orb} is high enough, lowish values of N_{pos} are acceptable as the radial distribution is sampled well enough to give a representative set of radii and velocities. We find that using $N_{\text{orb}} = 10^5$ and $N_{\text{pos}} = 10$ enables us

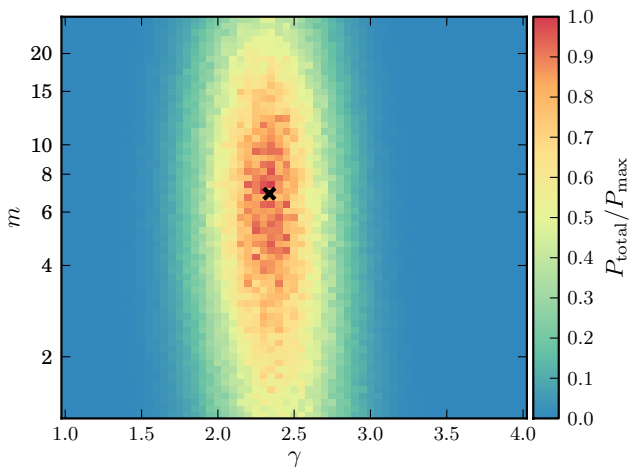


Figure 5. The likelihood of observing the M31 satellite system as a function of γ (which controls the distribution of semi-major axes) and m (which controls the distribution of orbital eccentricities). The black cross represents the most likely model as determined by marginalising over γ and m in turn.

to well sample the rv -space while keeping computing times down. The range of eccentricities sampled is $e \in [0, 1]$. For the semi-major axes, we have to take care. The timing argument assumptions break down very near to the centre of M31, so we do not allow a to become too small. To determine the range of semi-major axes, we take the 6.4 and 93.6 (1.5σ) percentiles of the combined separation-distance distributions, rounded to the nearest 50 kpc, to give $a \in [50, 450]$ kpc.

4.2 Satellite system

We search an 61×61 grid of models with $\gamma \in [1, 4]$ and $\ln m \in [0.25, 3.25]$, which corresponds to $m \in [1.3, 25.8]$. The sampling is performed logarithmically in m instead of linearly. The right panel of Fig. 2 shows that a change in m for small values of m has a more significant effect on the shape of the eccentricity distribution than for large values of m .

The total likelihood of observing the whole M31 satellite system is shown in Fig. 5 as a function of γ and m . The value of γ is well constrained in the range that we have considered indicating

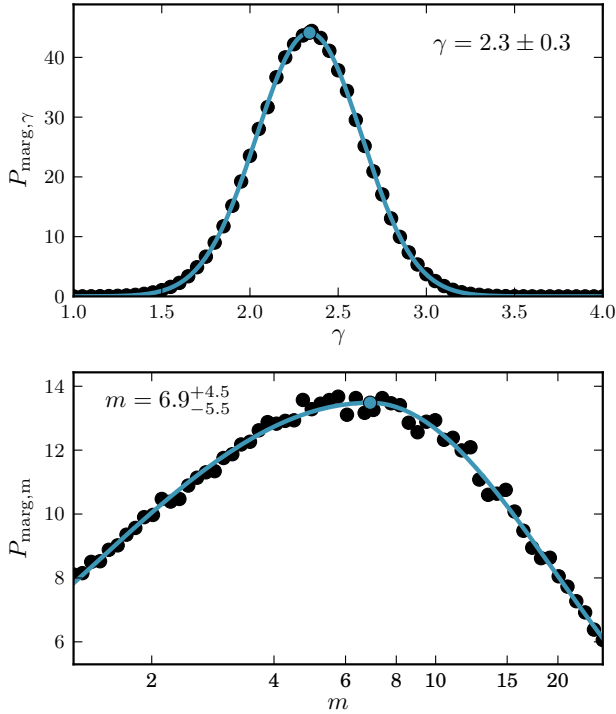


Figure 6. Marginalised likelihood of the M31 satellite system as a function of γ (left) and m (right). γ is tightly constrained at $\gamma = 2.5 \pm 0.3$. m shows more scatter but still reaches a clear peak at $m = 7.4^{+9.7}_{-8.4}$.

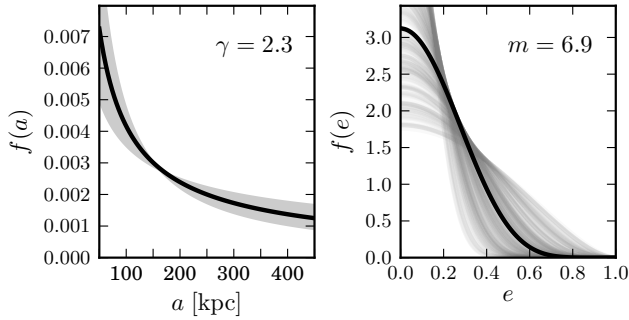


Figure 7. The distributions of semi-major axes and orbital eccentricity for the values of γ and m that best reproduce the M31 satellite system.

that there is a very specific distribution of semi-major axes that fit the observed satellite distribution. The distribution of eccentricities is less-well constrained; it is for this reason that we consider such a large range of m values. There is some scatter between models as N_{tot} is finite. To determine the values of γ and m that maximise the likelihood of the satellite system, we marginalise over m and γ in turn. The results are shown in Fig. 6, with an asymmetric Gaussian fitted to the marginalised points to determine the peak of the distribution. The top panel shows the marginalised likelihood as a function of γ and it is again clear that γ is well constrained. The bottom panel shows the marginalised likelihood as a function of m ; the constraints are weaker here but the distribution does reach a clear peak.

The best model, after marginalisation, is found to have $\gamma = 2.3 \pm 0.3$ and $m = 6.9^{+4.5}_{-5.5}$. This is marked with a black cross in Fig. 5. The corresponding orbital distribution functions are shown

in Fig. 7. From these, we can see that such a value for γ favours short semi-major axes, while still allowing a small number of large semi-major axis lengths (which are required for the outermost satellites). Such values for m strongly favour low eccentricities, and rule out higher eccentricities.

4.3 Individual satellites

Now we turn to the likelihoods of the individual satellites; these are shown as a function of γ and m in Fig. 8 with the satellites ordered according to the median of their separation distance distribution. The colours of the pixels represent the likelihood of the satellite in a given model; all the satellites are shown on the same likelihood (colour) scale to aid comparison. The best model for the entire satellite system is shown by the black cross in each panel. The best model for each individual satellite is shown as a white cross.

M32 appears to be unlikely for all of the models we have considered here, which is probably due to its proximity to M31; the example model shown in Fig. 3 clearly shows that very small separation distances are hard to achieve with the range of semi-major axes we have used. And XVIII, Pegasus and IC 1613 also appear to be rather unlikely, but in their case it is due to their large separation distances. And XXVII also has a low-likelihood. The large errors on its heliocentric distance (which arise because it is in the process of being tidally disrupted and may even be gravitationally unbound (Collins et al. 2012)) lead to a correspondingly large range of separation distances (see Fig. B1).

And XII and And XIV also have low likelihoods for all values of γ and m . We cannot make the same arguments for these satellites, as both are found at distances similar to the main bulk of the satellite population. It is their large line-of-sight velocities that make them unusual. This indicates that they are not well described by the models that we have been considering here. To apply the timing argument, we have made two assumptions: that the orbits are in the nearly-Keplerian regime; and that the Milky Way and other satellites make only a negligible contribution to the orbits. In the Monte Carlo simulations, we have made a third assumption that the satellites are part of a well-mixed population with orbits consistent with the distributions functions described in equation (4). We believe that the first assumption does hold good at these intermediate radii, and, in Section 1, we discussed our reasons for the second assumption in some detail. Thus, it is the third assumption that we suspect is invalid for these two satellites and we conclude that they are not part of a well-mixed population.

We observe a trend in the preferred value of γ with separations; the innermost satellites all favour high values of γ , that is, they require very small semi-major axes. Moving out in radius, the preferred value of γ shifts to lower values, allowing for increasing numbers of satellites with larger semi-major axes. For the outermost satellites, small values of γ are strongly preferred as these models necessarily allow orbits with large semi-major axes. The exception to this trend is And XXVII, but it has very large distance errors and should be treated with caution.

A sample of separations and line-of-sight velocities generated from the best model is shown in Fig. 9. Just as in Fig. 3, the points are coloured according to their number of nearest neighbours as an indication of the density. The positions and velocities of the satellites are also shown, with And XII, M32, And XIV, M32 and And XXVII marked. As we have already noted, M32 is very close in to M31 and the model has trouble producing satellites at such small distances. The very large uncertainty on the distance of And XXVII is

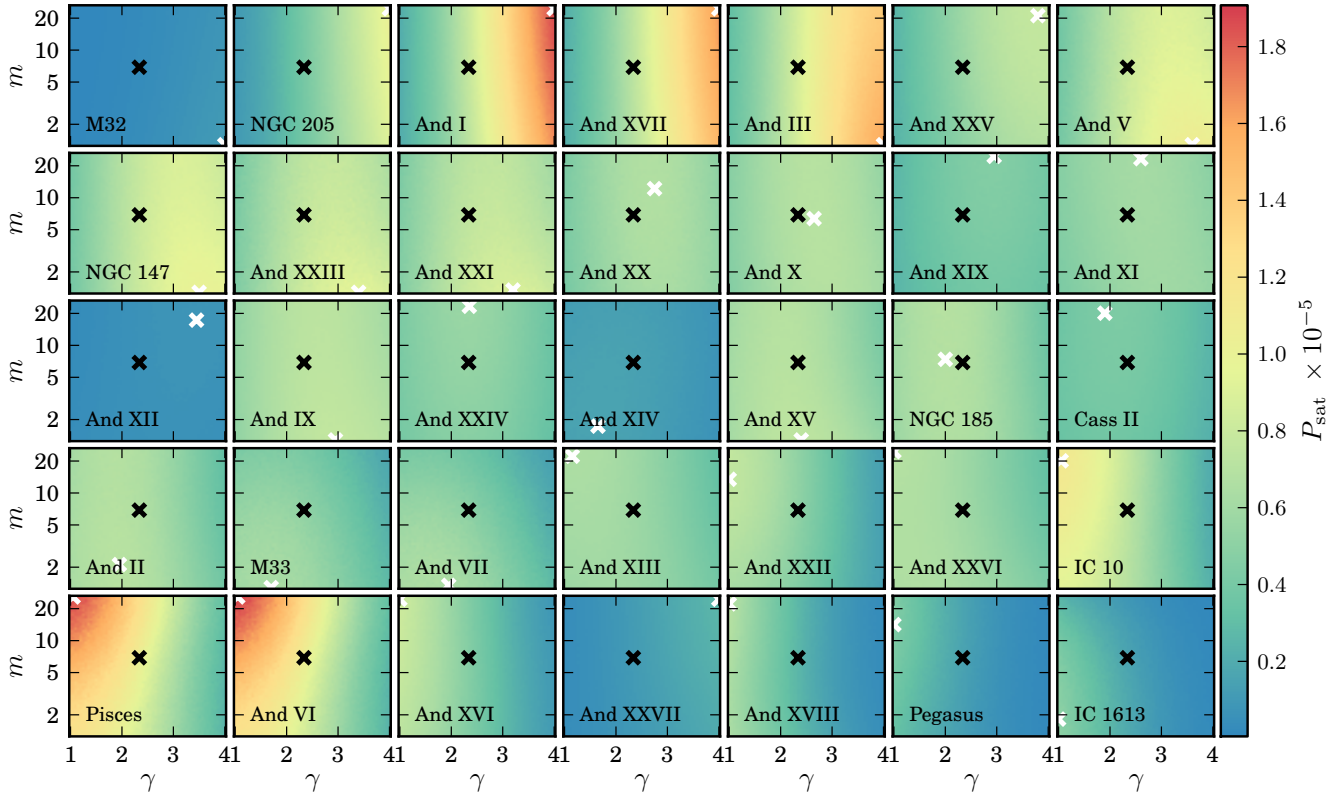


Figure 8. The likelihood of observing each M31 satellite as a function of the model parameters γ and m (which determine the distribution of semi-major axes and eccentricities respectively). The colours of the pixels indicate with likelihood, with all satellites plotted using the same scale to allow easy comparison. The satellites are ordered by the median of their separation distribution. Both And XII and And XIV have a very low likelihood for all models, despite having separations similar to the bulk of the satellite population, suggesting that they are very unusual objects.

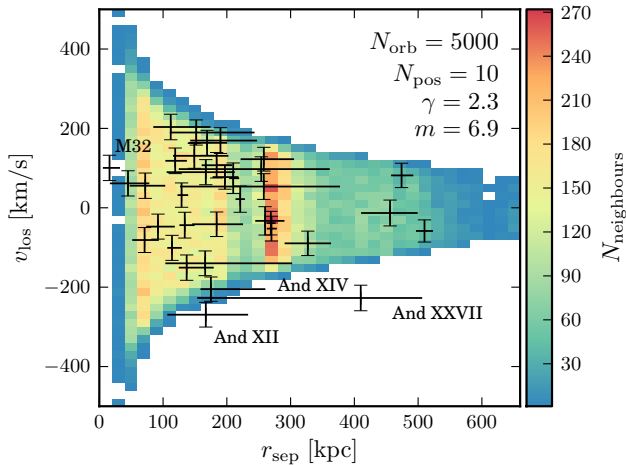


Figure 9. A sample of separations and line-of-sight velocities generated from the best model (for details see Fig. 3), with the observed values (and errors) for the satellites overplotted. And XII and And XIV are outliers to the model distribution, explaining their low likelihoods. M32 is also an outlier as there are few model orbits found at such low separations. And XXVII is also marked to highlight the very large uncertainty on its separation.

also apparent here. And XII and And XIV are very much outliers to the distribution of model points, which explains the low likelihoods that we recover.

4.4 Orbital properties

For each orbit i in a given model, we have a semi-major axis a and eccentricity e . From these, we can calculate the period T , apocentric distance r_a and pericentric distance r_p . Then for orbit parameter X , the weighted-mean period \bar{X}_{sat} of the satellite for that model is given by

$$\bar{X}_{\text{sat}}(\gamma, m) = \frac{\sum_{i=1}^N P(\Theta_{\text{sat}}|\Theta_i, \gamma, m) X_i}{\sum_{i=1}^N P(\Theta_{\text{sat}}|\Theta_i, \gamma, m)}. \quad (9)$$

The distributions of mean periods \bar{T}_{sat} are shown in Fig. 10. The mean period for all the models is shown in the upper-right corner of each plot. For all satellites, the average period changes very little over the range of models considered here. As expected, the periods of the satellite become larger as their separation from M31 increases. And XXVII is somewhat anomalous in having a very small period, whereas the satellites at similar distances have very long periods, but this is likely due to the fact that the errors on its heliocentric distance are large.

And XII and And XIV seem to have average periods consistent with those of their neighbours. The period of And XII is estimated at $\bar{T} \sim 3.5$ Gyr and the period of And XIV is estimated at $\bar{T} \sim 7$ Gyr. Thus, for these models, And XIV is predicted to be on its second or third orbit, and And XII on its fourth; i.e. neither satellite is on its first infall into the M31 system. However, from Fig. 8, we conclude that these satellites are unlikely for all of the models that

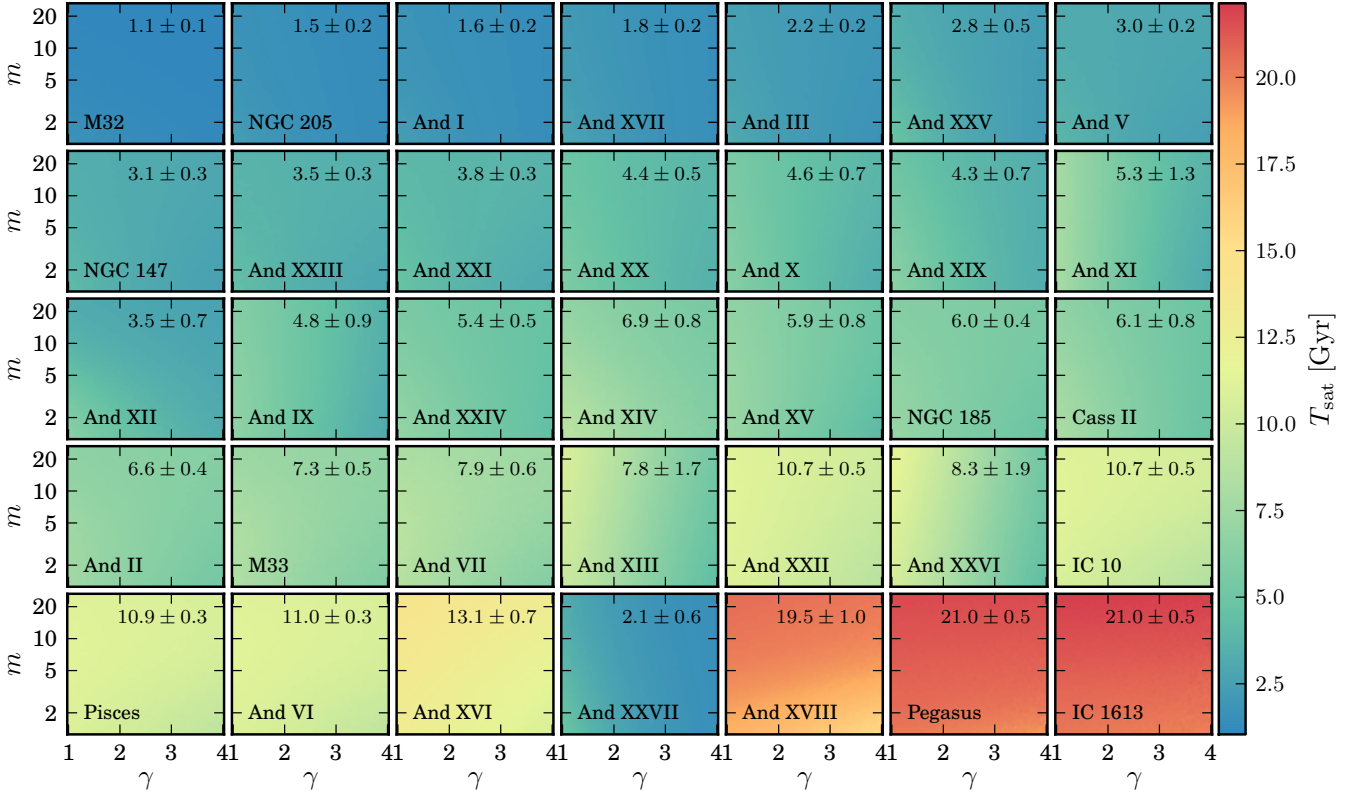


Figure 10. Weighted-mean orbital period as a function of model parameters γ and m for each satellite. The colours of the pixels indicate the mean period. The periods change significantly from satellite to satellite, generally increasing with separation. However the periods change little over the range of models considering, indicating that the mean period is a robust measure for each satellite. For each satellite, the mean period for all the models is shown in the top-right corner of each panel.

we have considered, so it is unwise to put too much faith into these periods.

We can go one step further and consider the mean orbital parameters of each satellite over all models that we have considered. To do this we take the weighted mean of the weighted-mean orbital parameter, using the model likelihoods for each satellite as the weights. For orbital parameter X , that is,

$$\langle \bar{X}_{\text{sat}} \rangle = \frac{\sum_{\gamma, m} P(\Theta_{\text{sat}}|\gamma, m) \bar{X}_{\text{sat}}(\gamma, m)}{\sum_{\gamma, m} P(\Theta_{\text{sat}}|\gamma, m)}. \quad (10)$$

Similarly, we calculate the weighted variance of the parameters to estimate the uncertainty on these values. We do this for each of the period, semi-major axis, eccentricity, apocentre and pericentre and for each satellite; the results are displayed in Table 2.

A number of orbits can reproduce a given separation distance and, whilst their semi-major axes are well constrained, their eccentricities can show more variation. Nonetheless, the weighted means of the eccentricities reported in Table 2 are all very similar, and are comparable to the means of the theoretical distributions in equation (4). Thus, this is a consequence of the assumption that the satellites are well-mixed and have a power-law density profile. If this assumption were dropped – for example, if the profile is broken – then the eccentricities would show greater variation.

The range of semi-major axes sampled by the distribution functions is [50, 450] kpc; we discussed the motivations for this choice in Section 4.1. Suppose we consider curtailing this range at the upper end and re-run our simulations over a coarse grid using

a range [50, 350] kpc. The innermost satellites are oblivious to this change. The outermost satellites (And XVIII, Pegasus and IC 1613) are significantly affected. For example, IC 1613 lies at a distance of 510 ± 12 kpc from the centre of M31. Orbits with semi-major axes $a \sim 450$ kpc need only be mildly eccentric to produce a satellite at this distance. Orbits with semi-major axes $a \sim 350$ kpc need to be more eccentric to reach out to ~ 500 kpc. So distribution functions with lower m are now preferred that permit more orbits with larger eccentricities. The predicted weighted means of the eccentricities for the outermost satellites do change significantly, namely $\bar{e} \sim 0.60$ for And XVIII, $\bar{e} \sim 0.87$ for Pegasus and $\bar{e} \sim 0.95$ for IC 1613.

5 INFALLING GROUPS

Using simulations of galaxy formation in a hierarchical merging cosmogony, Li & Helmi (2008) found that nearly a third of the dark matter subhalos were accreted in groups. Such behaviour is not unexpected. Sales et al. (2007) postulate that outlying satellites on extreme orbits may have been part of an infalling pair. When the pair interact with the host, the heavier member can maintain a bound orbit, but the lighter satellite is kicked out onto a high-energy orbit. Observations also show ample evidence for group infall; de Jong et al. (2010) recently presented evidence that Leo IV and Leo V could be a bound “tumbling pair” falling into the Milky Way and, in their discovery of And XXII, Martin et al. (2009) noted that it lies closer in projection to M33 than M31 and suggested that it

Table 2. Mean orbital properties for the M31 satellites.

	period (Gyr)	semi-major axis (kpc)	eccentricity	apocentre (kpc)	pericentre (kpc)
And I	1.6 ± 0.2	74 ± 4	0.21 ± 0.07	90 ± 8	59 ± 5
And II	6.6 ± 0.4	192 ± 8	0.23 ± 0.08	235 ± 17	148 ± 17
And III	2.2 ± 0.2	90 ± 6	0.23 ± 0.08	111 ± 10	70 ± 9
And V	3.0 ± 0.2	114 ± 6	0.23 ± 0.08	140 ± 9	88 ± 11
And VI	11.0 ± 0.3	273 ± 6	0.17 ± 0.05	320 ± 10	226 ± 18
And VII	7.9 ± 0.6	217 ± 11	0.28 ± 0.09	277 ± 19	157 ± 22
And IX	4.8 ± 0.9	152 ± 20	0.23 ± 0.08	186 ± 26	118 ± 20
And X	4.6 ± 0.7	149 ± 14	0.22 ± 0.07	181 ± 19	116 ± 16
And XI	5.3 ± 1.3	159 ± 26	0.22 ± 0.07	193 ± 32	125 ± 25
* And XII	3.5 ± 0.7	125 ± 15	0.21 ± 0.07	152 ± 27	98 ± 5
And XIII	7.8 ± 1.7	208 ± 32	0.22 ± 0.08	253 ± 37	163 ± 33
* And XIV	6.9 ± 0.8	197 ± 14	0.23 ± 0.06	243 ± 28	151 ± 9
And XV	5.9 ± 0.8	177 ± 15	0.23 ± 0.08	217 ± 21	136 ± 21
And XVI	13.1 ± 0.7	305 ± 11	0.22 ± 0.07	371 ± 13	240 ± 29
And XVII	1.8 ± 0.2	79 ± 6	0.21 ± 0.07	95 ± 10	62 ± 7
* And XVIII	19.5 ± 1.0	400 ± 15	0.22 ± 0.08	487 ± 16	313 ± 44
And XIX	4.3 ± 0.7	141 ± 15	0.20 ± 0.06	170 ± 22	112 ± 12
And XX	4.4 ± 0.5	145 ± 10	0.21 ± 0.07	176 ± 15	114 ± 12
And XXI	3.8 ± 0.3	133 ± 7	0.24 ± 0.08	165 ± 11	102 ± 14
And XXII	10.7 ± 0.5	267 ± 9	0.20 ± 0.06	322 ± 14	213 ± 20
And XXIII	3.5 ± 0.3	127 ± 6	0.24 ± 0.09	157 ± 10	97 ± 13
And XXIV	5.4 ± 0.5	167 ± 10	0.20 ± 0.06	202 ± 18	133 ± 12
And XXV	2.8 ± 0.5	108 ± 11	0.20 ± 0.06	130 ± 16	85 ± 10
And XXVI	8.3 ± 1.9	216 ± 36	0.23 ± 0.08	265 ± 43	168 ± 38
* And XXVII	2.1 ± 0.6	85 ± 14	0.19 ± 0.06	101 ± 19	69 ± 10
Cass II	6.1 ± 0.8	181 ± 15	0.21 ± 0.06	218 ± 24	144 ± 14
IC 10	10.7 ± 0.5	268 ± 9	0.21 ± 0.07	323 ± 12	212 ± 24
* IC 1613	21.0 ± 0.5	422 ± 7	0.31 ± 0.06	552 ± 15	293 ± 29
* M32	1.1 ± 0.1	60 ± 3	0.27 ± 0.10	77 ± 9	44 ± 4
M33	7.3 ± 0.5	206 ± 9	0.27 ± 0.08	261 ± 19	151 ± 18
NGC 147	3.1 ± 0.3	117 ± 6	0.23 ± 0.08	144 ± 10	90 ± 11
NGC 185	6.0 ± 0.4	180 ± 8	0.22 ± 0.07	220 ± 16	141 ± 15
NGC 205	1.5 ± 0.2	72 ± 4	0.21 ± 0.07	87 ± 8	57 ± 5
* Pegasus	21.0 ± 0.5	423 ± 6	0.19 ± 0.05	504 ± 12	342 ± 24
Pisces	10.9 ± 0.3	272 ± 6	0.18 ± 0.05	319 ± 10	224 ± 18

Notes: * Objects are unlikely to be correctly described by the class of models used to generate these orbital properties and should be used with caution.

could be a satellite of M33. With orbital properties for all of the M31 satellites, it is worth taking a moment to consider whether there is any evidence that groups of satellites can be associated and may have had a common origin.

First we consider whether And XXII ($a = 267 \pm 9$ kpc, $e = 0.20 \pm 0.06$) might be not a satellite of M31 but of M33, which itself has parameters $a = 206 \pm 9$ kpc, $e = 0.27 \pm 0.08$. Tollerud et al. (2012) and Chapman et al. (2012) both found radial velocities consistent with this hypothesis. The latter authors analysed N-body simulations of the M31-M33 system, which suggest that And XXII may indeed be a satellite of M33. We find that the semi-major axes are not similar, from which we conclude that the two satellites are not moving independently along the same orbit; but whether this means they are orbiting each other or are unrelated, we cannot determine from this analysis.

NGC 147 ($a = 117 \pm 6$ kpc, $e = 0.23 \pm 0.08$) and NGC 185 ($a = 180 \pm 8$ kpc, $e = 0.22 \pm 0.07$) are very close together on the sky and a connection between them has long been suspected. However the orbits we find for these two objects in our study do not support such a conclusion. Their eccentricities are similar, but their semi-major axes are quite different, so much so that NGC 147 com-

pletes two orbits in the time that NGC 185 takes to complete one. Recent discovery Cass II ($a = 181 \pm 15$ kpc, $e = 0.21 \pm 0.06$) lies close to this pair and could be a third member of their subsystem, if such a subsystem exists (see e.g., Irwin et al. 2012). Collins et al. (2012) argue that a connection is possible based on the line-of-sight velocity they measure for Cass II. Our results certainly favour a connection between Cass II and NGC 185 as the orbital parameters we find for them are in close agreement, but not for Cass II and NGC 147.

To find other possible infalling groups, we select satellites with semi-major-axis and eccentricity estimates that overlap within their errors. This gives us 47 pairs of satellites. We further require that the pairs be in close proximity, namely less than 100 kpc apart. This corresponds to an angle of 7.4° at the distance of M31, so we keep only pairs with separations smaller than this value. This leaves us with 14 pairs (of which eight are individual pairs and the rest form two groups of three). Finally, we calculate separation profiles for each of these pairs and calculate the median separation distance. We reject all pairs with median separation larger than 100 kpc, to obtain three candidate pairs and one candidate group, of which the Cass II - NGC 185 pair (separation 46^{+32}_{-29} kpc)

has already been discussed. The other two pairs are: And I ($a = 74 \pm 4$ kpc, $e = 0.21 \pm 0.07$) and And XVII ($a = 79 \pm 6$ kpc, $e = 0.21 \pm 0.07$), which have a separation 84_{-3}^{+9} kpc; and And IX ($a = 152 \pm 20$ kpc, $e = 0.23 \pm 0.08$) and And X ($a = 149 \pm 14$ kpc, $e = 0.22 \pm 0.07$), which have a separation 61_{-24}^{+38} kpc. The group is composed of And V ($a = 114 \pm 6$ kpc, $e = 0.23 \pm 0.08$), And XXV ($a = 108 \pm 11$ kpc, $e = 0.20 \pm 0.06$) and NGC 147; the And V-And XXV separation is 95_{-9}^{+42} kpc, the And V-NGC 147 separation is 84_{-4}^{+5} kpc and the And XXV-NGC 147 separation is 41_{-14}^{+43} kpc. Further study is required to determine whether these candidate groups are real.

6 MINIMUM-MASS SOLUTIONS

In the modelling, we assumed that all of the satellites are part of a well-mixed population described by the distribution functions in equation (4). We believe it is this assumption that is not appropriate for And XII and And XIV. Here, we relax that assumption and then use the timing argument to analyse the orbits of these two satellites, placing no priors on the orbital properties.

6.1 The timing argument revisited

In Section 3.1, we already outlined the timing argument (equation (1)). There are four equations and four unknowns (a , e , M and η). Apart from the special case $e = 1$, these equations must be solved numerically to yield multiple solutions corresponding to increasing numbers of pericentric passages. To proceed, we combine the equations to eliminate a , e and M :

$$t = \frac{r \left(|v_r| \eta \sin \eta \left[v_r^2 + v_t^2 \sin^2 \eta \right]^{\frac{1}{2}} - v_r^2 \sin^2 \eta \right)}{v_r \left(\left[v_r^2 + v_t^2 \sin^2 \eta \right]^{\frac{1}{2}} - |v_r| \cos \eta \right)}. \quad (11)$$

To solve equation (11) for η , we must provide t , r , v_r and v_t at the present time. As before, we assume $t = t_u$, the age of the universe (see Section 3.1). The remainder of the parameters may be estimated from position and velocity data of M31 and the satellites. The separations r are calculated using trigonometry from the heliocentric distances and positions (equation (5)). The velocities v_r and v_t have contributions from both the line-of-sight velocities and the proper motions, both of which must be corrected for the solar peculiar motion, motion of the LSR and the relative motion of the Milky Way and M31 (see Section 3.3). However, as we do not have proper motion estimates for the satellites, we cannot compute either v_r or v_t ; instead we model to account for this incomplete data.

The corrected line-of-sight velocities v_{cor} of the satellites in the M31 frame have contributions from both the radial velocities v_r and the tangential velocities v_t referred to the centre of M31,

$$v_{\text{cor}} = v_r \cos \alpha + v_t \sin \alpha \cos \xi, \quad (12)$$

where α is the angle between the line joining the centre of M31 to the centre of the dSph and the line-of-sight to the dSph, and ξ the angle between the tangential velocity vector and the plane containing M31, the dSph and the Sun. Now, α may be calculated via

$$\cos \alpha = \frac{d^2 + r^2 - d_{\text{M31}}^2}{2dr}, \quad \sin \alpha = \frac{d_{\text{M31}} \sin \theta}{r}, \quad (13)$$

where θ is the angular separation of the dSph and M31 on the sky. It is convenient to introduce the (positive) velocity ratio $R = v_t/|v_r|$, such that

$$v_t = \frac{R v_{\text{cor}}}{\text{sign}(v_r) \cos \alpha + R \sin \alpha \cos \xi}. \quad (14)$$

There is no available data on the velocity ratio R and the angle of inclination of the orbit with respect to the plane of the sky ξ . Even so, the solution corresponding to the minimum mass M is well-defined. A little consideration shows that on physical grounds, the orbit's kinetic energy – and hence the total mass – is minimised if $\xi = 0$ (for $v_{\text{cor}} > 0$) and if $\xi = \pi$ (for $v_{\text{cor}} < 0$, which is the case for And XII and And XIV). A good approximation to the value of R for the minimum mass is given by minimising the Lagrangian L

$$L = \frac{1}{2} (v_r^2 + v_t^2) - \ell (v_r \cos \alpha - v_t \sin \alpha - v_{\text{cor}}) \quad (15)$$

where ℓ is the Lagrange multiplier. This leads to the solution $R = \tan \alpha$. In fact, though this is a good physical guide to the location of the solution, it is not exact. However, it provides a good starting point for a grid search, in which for successive R values, equation (11) is solved for η iteratively and the minimum mass is located.

6.2 Results

We start by searching for a solution $\eta \in [\pi, 2\pi]$, thus assuming that the dwarfs are on their first infall into M31 (multiple pericentric passages necessarily imply higher masses). For And XII we are able to place a lower constraint on the mass of the system of $M \geq 2.1 \times 10^{12} M_\odot$, corresponding to $R = 0.6$. Similarly for And XIV, there is a minimum mass estimate of $M \geq 1.1 \times 10^{12} M_\odot$ when $R = 4.3$. The corresponding orbital parameters are given in Table 3. Although our primary aim here is to understand the orbits of And XII and And XIV, we note that these are in reasonable agreement with earlier mass estimates $M = 1.23_{-0.6}^{+1.8} \times 10^{12} M_\odot$ (Evans & Wilkinson 2000; Evans et al. 2000) and $M = 1.5 \pm 0.4 \times 10^{12} M_\odot$ (Watkins et al. 2010). Remember that these are minimum mass solutions that we have adopted here; higher mass solutions exist, however moving away from this minimum would quickly result in unfeasibly high mass estimates for M31, so we are confident that the orbital parameters will be close to the values predicted by this analysis. The resulting orbit of And XII is highly eccentric, it has an eccentricity $e \sim 0.9$ with a corresponding pericentre distance of only a few kiloparsecs. The orbit of And XIV is of a more moderate eccentricity and puts And XIV very near pericentre at the current time, which would explain its high velocity.

We now repeat the analysis for solutions corresponding to multiple pericentric passages. The results for the first four solutions are shown in Fig. 11, with the upper set of graphs pertaining to And XII and the lower set to And XIV. The left panels show the apocentres, pericentres and semi-major-axis lengths of the orbits. The top-right panels show that the mass estimate increases with increasing numbers of pericentric passages. The corresponding orbital properties are given in Table 3. Again for And XII, all of these orbits are highly eccentric with small pericentre distances; this poses a problem for solutions that allow for more than one pericentre passage. We would expect such close encounters with M31 to result in a significant amount of tidal distortion, but there is little evidence for such an interaction around either satellite. Furthermore, the mass estimates for the system (already high for the first solution) become very high for subsequent solutions. From this, we conclude that And XII cannot have passed through pericentre and, thus, must be on its first infall. For And XIV, it is less certain that we can rule out multiple-orbit scenarios; all four solutions predict

Table 3. Orbital parameters resulting from the timing argument analyses.

	solution	semi-major axis (kpc)	eccentricity	mass ($\times 10^{12} M_{\odot}$)	apocentre (kpc)	pericentre (kpc)	period (Gyr)
And XII	1	364	0.90	2.1	690	38	14.3
	2	244	0.87	2.5	455	32	7.1
	3	196	0.86	2.9	364	28	4.7
	4	170	0.86	3.4	315	24	3.5
And XIV	1	292	0.49	1.1	436	148	14.2
	2	199	0.30	1.3	258	140	7.2
	3	163	0.20	1.6	195	130	4.9
	4	142	0.23	2.1	175	109	3.7

masses consistent with previous estimates and the orbits are all reasonable on observational grounds.

So far, this analysis has used a single estimate for the separation distance and line-of-sight velocity of the satellite, and does not account for any uncertainties in these measurements, which we know to be considerable in some cases. As discussed in Section 2, we now use full separation profiles and assume that the line-of-sight velocities have Gaussian errors. We select 10^3 separations r and line-of-sight velocities v_{los} from these distributions and perform the same minimum-mass analysis, now requiring that the satellites are on their first infall. The median and 1-sigma uncertainties in the minimum mass estimates are $M = 1.9_{-0.8}^{+1.0} \times 10^{12} M_{\odot}$ for And XII and $M = 1.3_{-0.2}^{+0.8} \times 10^{12} M_{\odot}$ for And XIV. The full distributions of minimum mass estimates are shown in Fig. 12 with And XII in red and And XIV in blue; the solid (dotted) lines show the best estimate (uncertainties) from Watkins et al. (2010). Both mass distributions are consistent with this mass estimate. Indeed, the And XII distribution agrees very well with previous estimates, supporting the idea that And XII must be on its first infall into the M31 system. The And XIV mass distribution, on the other hand, shows two distinct peaks. This is a direct consequence of the double-peaked heliocentric distance profile from Conn et al. (2012), such that smaller heliocentric distances produced larger host-satellite separations and thus, higher mass estimates. (Subsequent solutions assuming multiple pericentric passages produce minimum-mass profiles of similar shapes shifted to higher masses.) The low-mass peak contains low and moderate eccentricity orbits, with large pericentre distances, so solutions admitting multiple pericentre passages would be feasible; the high-mass peaks correspond to orbits of higher eccentricity and lower pericentre distance, such that we could make the same arguments as we did earlier for And XII and say that And XIV cannot have passed through pericentre. As such, even in the absence of proper motion data, improved distance estimates are required to make any conclusion about And XIV via this analysis.

7 CONCLUSIONS

We have used the timing argument to study the orbits of the satellites of M31. In all previous timing argument studies, the Milky Way has formed one half of the pair under consideration; never before has the timing argument been applied to two external galaxies as we do here. Two satellites, And XII and And XIV, are of particular interest as they are believed to be on their first infall into the M31 system as they have very high line-of-sight velocities, higher than would be expected at their respective distances from M31.

As we lack transverse velocity information for the satellites, we cannot recover their orbits exactly. Instead we use Monte Carlo simulations to model the information that we do not have. We generate a series of orbits from physically-motivated distribution function and “observe” each orbit from a random viewing position. We then use Bayesian analysis to determine the likelihood of each satellite given the set of orbits generated for each distribution function.

In order to apply the timing argument, we have assumed that the orbits are nearly-Keplerian, that the Milky Way and other satellites have a negligible effect on the orbits and that the orbits are part of a smooth, well-mixed population. For the majority of the satellites, the models can recover the satellites very well and these assumptions hold. However, And XII and And XIV are both very poorly fit by any of the models we have considered here; they are indeed unusual, as their velocities suggest. Li & White (2008) showed that the timing argument performs well on a host-satellite system, even with the presence of a nearby Milky-Way-like companion for the host, and their distances put them well within the bulk of the satellite population where we would not expect the nearly Keplerian assumption to break down. Thus, we conclude that it is the final assumption that is incorrect, indicating that they are not well fit by a smooth distribution function. From this it is reasonable to conclude that they are on their first infall into the M31 system, or that they are recent ejections from the system after a three-body encounter (Sales et al. 2007).

In the light of this result, we relax the assumption that the orbits of And XII and And XIV are part of a well-mixed population and use the observed satellite properties to estimate their orbital parameters. Again, due to the lack of transverse velocities, we cannot do this exactly; instead we are forced to search over a grid of possible transverse velocity measurements and adopt the minimum mass solution. From this, we find that the And XII orbit solution is realistic only when we assume that it is on its first infall; the orbit we predict is highly eccentric with a pericentre distance that will bring it close to the centre of M31. For And XIV, we cannot rule out multiple pericentric passages; improved distance determination is needed to determine the most likely solution. Both satellites predict M31 masses consistent with previous studies.

Finally, we consider whether the satellites might be infalling in groups. We find four candidate groups (three pairs and one triple system), but further work is needed to confirm these predictions. Our results favour an association between Cass II and NGC 185, though not for NGC 185 and NGC 147, which have often been associated in the past. Other possible candidates for group infall in-

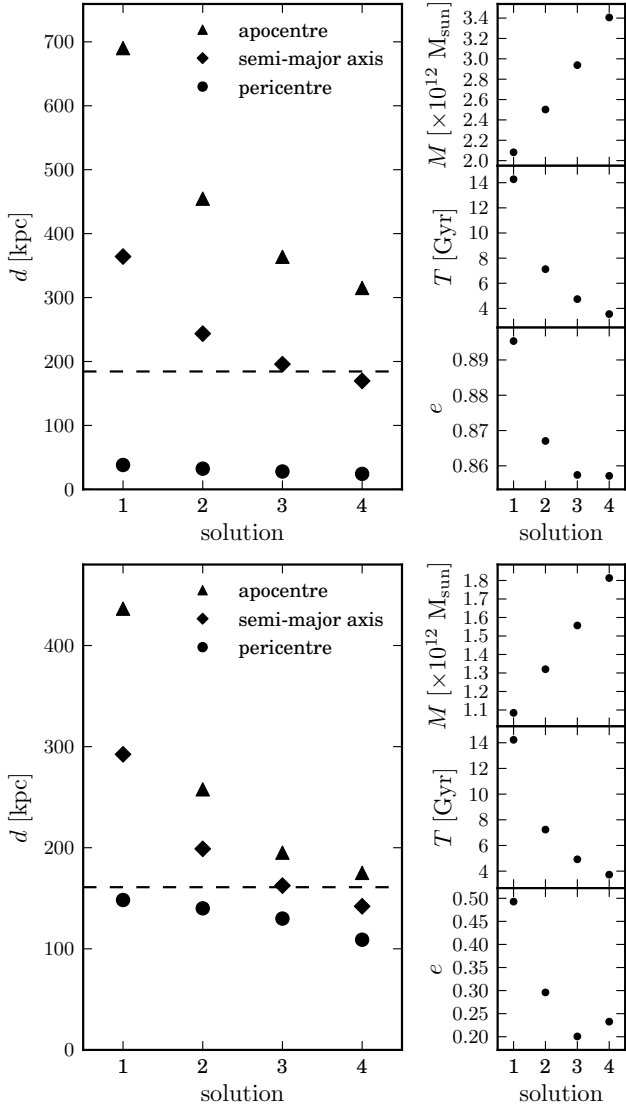


Figure 11. The first 4 η solutions for And XII (top set) and And XIV (bottom set). Left: apocentre (triangles), semi-major axis (diamonds) and pericentre (circles) as a function of solution number. The dotted line shows the current position of the satellite. It appears that the apocentre asymptotes to the current position of the satellite while the pericentre asymptotes to 0. Top right: Minimum mass estimate M as a function of solution number. Middle right: orbital period T as a function of solution number. Bottom right: eccentricity e as a function of solution number.

clude the pair And I and And XVII; the pair And IX and And X; and the triple And V, And XXV and NGC 147.

In this paper we have studied the M31 satellites. However, the method we have used is also readily applicable to the Milky Way satellite system. It would be particularly interesting to compare the phase-space distribution function favoured by the Milky Way system with that predicted here, and to study the orbits of the Milky Way satellites with their M31 counterparts. We could also use this method to investigate whether the ultrafaint dwarf spheroidals are kinematically different to the classical dwarf spheroidals.

We need not limit analyses of this nature to such massive hosts; we have already discussed the growing body of evidence that And XXII is not a satellite of M31 but of M33 and there are

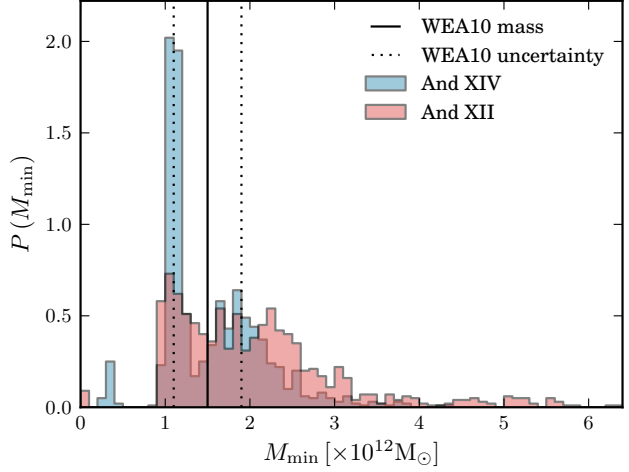


Figure 12. The distribution of minimum mass estimates for And XII (red histogram) and And XIV (blue histogram). The solid and dotted lines show the best M31 mass estimate and the uncertainties from Watkins et al. (2010).

two extended clusters, EC 1 and EC 2, that are also found in close proximity to M33. The techniques we have developed here could also be applied to this system to study their orbital properties and determine if the proposed satellites are truly bound to M33.

We are grateful to Anthony Conn and Michelle Collins for making their distance profiles and velocity measurements available in advance of publication, and to David Hogg for interesting (and very useful) discussions.

REFERENCES

- Bell E. F., Slater C. T., Martin N. F., 2011, *ApJ*, 742, L15
 Bender R., Paquet A., Nieto J.-L., 1991, *A&A*, 246, 349
 Brasseur C. M., Martin N. F., Rix H.-W., Irwin M., Ferguson A. M. N., McConnachie A. W., de Jong J., 2011, *ApJ*, 729, 23
 Chapman S. C. et al., 2007, *ApJ*, 662, L79
 Chapman S. C. et al., 2012, *ArXiv e-prints*
 Cole A. A. et al., 1999, *AJ*, 118, 1657
 Collins M. L. M. et al., 2010, *MNRAS*, 407, 2411
 Collins et al. 2012, submitted
 Conn A. R. et al., 2012, *ArXiv e-prints*
 Courteau S., van den Bergh S., 1999, *AJ*, 118, 337
 de Jong J. T. A., Martin N. F., Rix H., Smith K. W., Jin S., Macciò A. V., 2010, *ApJ*, 710, 1664
 Dehnen W., Binney J. J., 1998, *MNRAS*, 298, 387
 Evans N. W., Hafner R. M., de Zeeuw P. T., 1997, *MNRAS*, 286, 315
 Evans N. W., Wilkinson M. I., 2000, *MNRAS*, 316, 929
 Evans N. W., Wilkinson M. I., Guhathakurta P., Grebel E. K., Vogt S. S., 2000, *ApJ*, 540, L9
 Fiorentino G., Contreras Ramos R., Tolstoy E., Clementini G., Saha A., 2012, *A&A*, 539, A138
 Huchra J. P., Vogeley M. S., Geller M. J., 1999, *ApJS*, 121, 287
 Huchtmeier W. K., Karachentsev I. D., Karachentseva V. E., 2003, *A&A*, 401, 483
 Ibata R., Martin N. F., Irwin M., Chapman S., Ferguson A. M. N., Lewis G. F., McConnachie A. W., 2007, *ApJ*, 671, 1591
 Irwin M. J., Ferguson A. M. N., Huxor A. P., Tanvir N. R., Ibata R. A., Lewis G. F., 2008, *ApJ*, 676, L17
 Irwin et al. 2012, in prep

Table A1. M32 distance modulus estimates; the method used to obtain each estimate is also given, along with the source.

$\mu \pm \sigma$	method	reference
24.55 ± 0.08	SBF	Tonry et al. (2001)
24.39 ± 0.08	SBF	Jensen et al. (2003)
24.53 ± 0.12	Red Clump	Monachesi et al. (2011)
24.42 ± 0.12	RR Lyraes	Sarajedini et al. (2012)
24.33 ± 0.21	RR Lyraes	Fiorentino et al. (2012)

Jensen J. B., Tonry J. L., Barris B. J., Thompson R. I., Liu M. C., Rieke M. J., Ajhar E. A., Blakeslee J. P., 2003, *ApJ*, 583, 712
Kahn F. D., Woltjer L., 1959, *ApJ*, 130, 705
Kalirai J. S. et al., 2010, *ApJ*, 711, 671
Kallivayalil N., Besla G., Sanderson R., Alcock C., 2009, *ApJ*, 700, 924
Karachentsev I. D., Karachentseva V. E., Huchtmeier W. K., Makarov D. I., 2004, *AJ*, 127, 2031
Kerr F. J., Lynden-Bell D., 1986, *MNRAS*, 221, 1023
Li Y., Helmi A., 2008, *MNRAS*, 385, 1365
Li Y., White S. D. M., 2008, *MNRAS*, 384, 1459
Majewski S. R. et al., 2007, *ApJ*, 670, L9
Martin N. F., Ibata R. A., Irwin M. J., Chapman S., Lewis G. F., Ferguson A. M. N., Tanvir N., McConnachie A. W., 2006, *MNRAS*, 371, 1983
Martin N. F. et al., 2009, *ApJ*, 705, 758
McConnachie A. W. et al., 2008, *ApJ*, 688, 1009
McConnachie A. W., Irwin M. J., Ferguson A. M. N., Ibata R. A., Lewis G. F., Tanvir N., 2005, *MNRAS*, 356, 979
Monachesi A., Trager S. C., Lauer T. R., Freedman W., Dressler A., Grillmair C., Mighell K. J., 2011, *ApJ*, 727, 55
Richardson J. C. et al., 2011, *ApJ*, 732, 76
Sakai S., Madore B. F., Freedman W. L., 1999, *ApJ*, 511, 671
Sales L. V., Navarro J. F., Abadi M. G., Steinmetz M., 2007, *MNRAS*, 379, 1475
Sarajedini A., Yang S.-C., Monachesi A., Lauer T. R., Trager S. C., 2012, *MNRAS*, 425, 1459
Slater C. T., Bell E. F., Martin N. F., 2011, *ApJ*, 742, L14
Spergel D. N. et al., 2007, *ApJS*, 170, 377
Strigari L. E., Bullock J. S., Kaplinghat M., Simon J. D., Geha M., Willman B., Walker M. G., 2008, *Nature*, 454, 1096
Tollerud E. J. et al., 2012, *ApJ*, 752, 45
Tonry J. L., Dressler A., Blakeslee J. P., Ajhar E. A., Fletcher A. B., Luppino G. A., Metzger M. R., Moore C. B., 2001, *ApJ*, 546, 681
van der Marel R. P., Fardal M., Besla G., Beaton R. L., Sohn S. T., Anderson J., Brown T., Guhathakurta P., 2012, *ApJ*, 753, 8
van der Marel R. P., Guhathakurta P., 2008, *ApJ*, 678, 187
Watkins L. L., Evans N. W., An J. H., 2010, *MNRAS*, 406, 264
Zucker D. B. et al., 2004, *ApJ*, 612, L121
Zucker D. B. et al., 2007, *ApJ*, 659, L21

APPENDIX A: DISTANCE TO M32

There have been a number of attempts to measure the heliocentric distance of M32 in recent years, using a variety of different methods, including RR Lyrae variables, surface brightness fluctuations and Red Clump stars. These distance modulus estimates are given in Table A1, along with the method that was used to obtain the estimates and their references. Faced with so many estimates, all of which result from careful, reliable studies, it is not clear which estimate should be adopted as the distance to M32; indeed different authors adopt different distance estimates in any M32 studies they undertake, and in some cases, studies simply adopt the same distance for M32 as they take for M31.

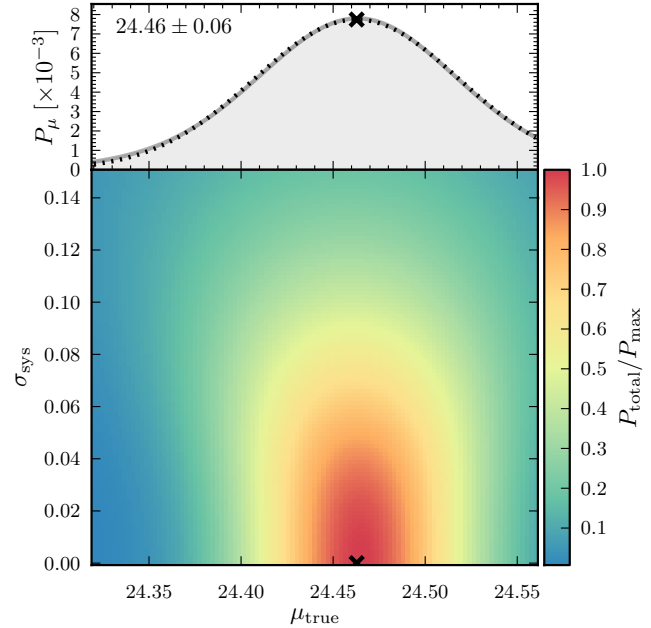


Figure A1. Bottom panel: The probability of observing the measured M32 distance moduli given their error estimates as a function of the true distance modulus μ_{true} and the systematic error σ_{sys} . Top panel: The marginalised probability for true distance modulus μ_{true} . The point at which the probability is maximised is marked with a cross.

All of these different methods have their advantages and disadvantages, with no one method being preferred over another; on the contrary, we are lucky to have so many different estimates from so many different data sets. Taken together, the estimates complement and support each other, and their overall agreement is remarkable. Instead of picking one distance estimate and ignoring the rest, we would like to use a value that takes into account all of the information in Table A1. To that end, here we present a statistical analysis that attempts to combine the previous estimates to obtain an improved distance estimate.

The most straightforward option would be to take a simple mean and use the standard deviation as the uncertainty. However, this does not take into account any uncertainties on the estimates themselves, only their scatter, and can be unreliable when the number of estimates is very small. A weighted mean - using weights equal to the inverse square of the uncertainties - would neatly address the first point, but not the second. Instead we turn to blind deconvolution, which is robust even with a small number of original estimates. We can also fit for an extra, as-yet-ignored systematic error on all the measurements.

To start, consider a set of distance-modulus estimates μ_i , each with uncertainty σ_i . Let us assume that there is a true distance modulus μ_{true} . Let us further assume that there is a systematic error σ_{sys} on each measurement that has not yet been accounted for in the quoted measurements such that the uncertainties on the measurements become

$$\sigma_i^* = \sqrt{\sigma_i^2 + \sigma_{\text{sys}}^2}. \quad (\text{A1})$$

Now the probability of observed measurement μ_i given the uncertainties and the true value is given by

$$P(\mu_i | \sigma_i, \sigma_{\text{sys}}, \mu_{\text{true}}) = \frac{1}{\sqrt{2\pi}\sigma_i^*} \exp\left(-\frac{(\mu_i - \mu_{\text{true}})^2}{2\sigma_i^{*2}}\right). \quad (\text{A2})$$

The probability of obtaining all measurements $\{\mu_i\}$ is then

$$\begin{aligned}
 & P\left(\{\mu_i\}_{i=1}^N \mid \{\sigma_i\}_{i=1}^N, \sigma_{\text{sys}}, \mu_{\text{true}}\right) \\
 &= \prod_{i=1}^N P(\mu_i \mid \sigma_i, \sigma_{\text{sys}}, \mu_{\text{true}}) \\
 &= \prod_{i=1}^N \frac{1}{\sqrt{2\pi}\sigma_i^*} \exp\left(-\frac{(\mu_i - \mu_{\text{true}})^2}{2\sigma_i^{*2}}\right). \quad (\text{A3})
 \end{aligned}$$

We calculate this probability over a grid of models with $\mu_{\text{true}} \in [24.32, 24.56]$ and $\sigma_{\text{sys}} \in [0, 0.15]$. The results of this grid search are shown in the bottom panel of Fig. A1, the colours of the pixels indicate the probability of a given $(\mu_{\text{true}}, \sigma_{\text{sys}})$ pair, with red representing high probability and blue representing low probability. The distribution peaks at a value of σ_{sys} close to 0, implying that there are no further systematic errors that must be taken into account in this case. The statistical error σ_{sys} is a nuisance parameter here; we must consider the possibility that there is an extra source of error on the estimates, however we are not interested in its value. It is the value of μ_{true} that we wish to determine. So we marginalise over σ_{sys} (top panel of Fig. A1) and adopt the value of μ_{true} at which the marginalised probability is maximised as the best estimate for the distance modulus. From the marginalised distribution for μ_{true} , we obtain an estimate $\mu_{\text{true}} = 24.46 \pm 0.06$, which corresponds to a distance of $d = 781 \pm 20$ kpc.

APPENDIX B: SEPARATION-DISTANCE DISTRIBUTIONS

Fig. B1 shows the complete set of separation-distance distributions that were used for this analysis.

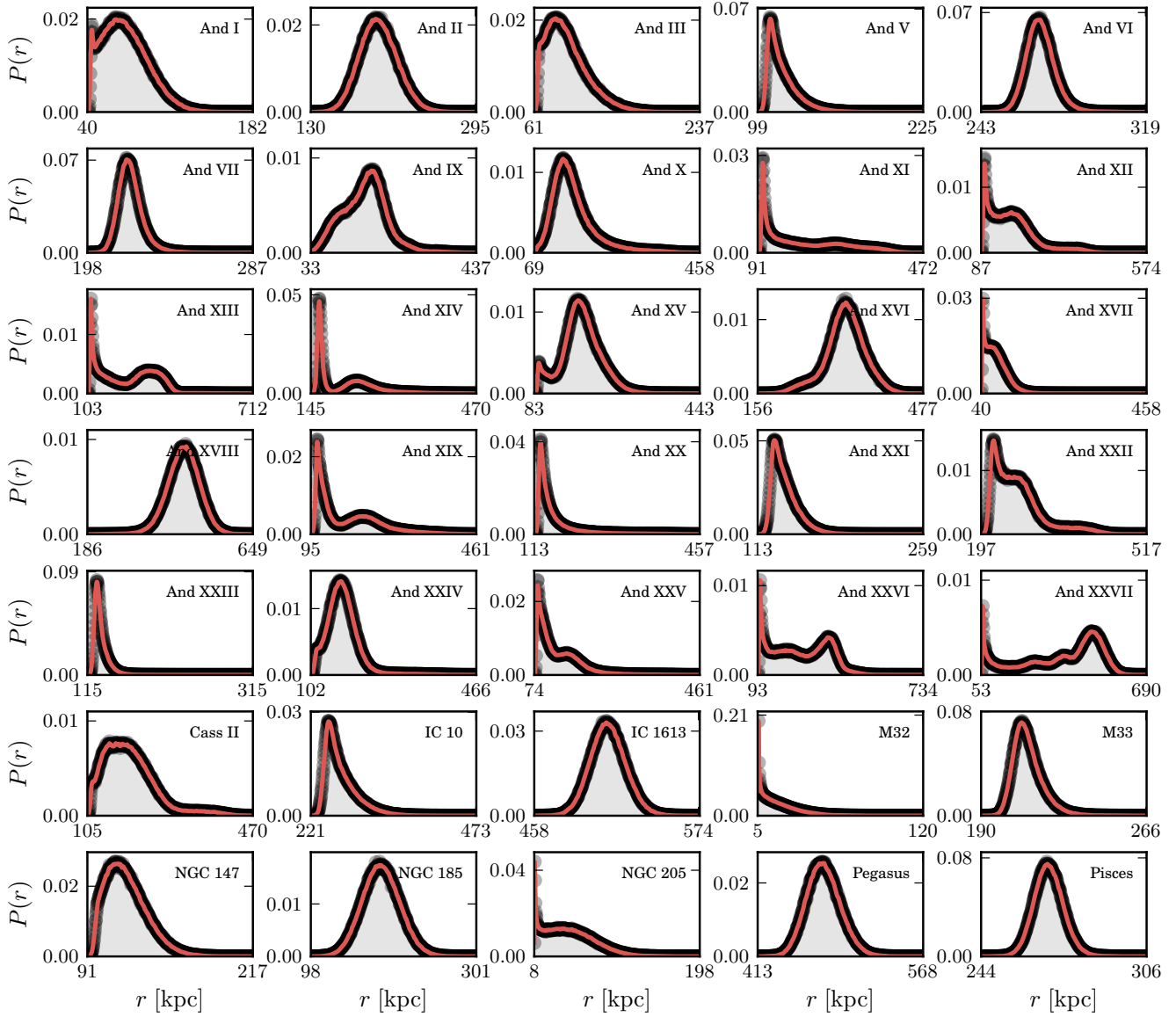


Figure B1. The distribution of separation distances for each of the M31 satellites. For satellites that are far enough away from the centre of M31 or have small errors on their distance, the Gaussian errors on the heliocentric distance result in Gaussian errors on the separation distances. For other satellite, the distribution finds a minimum separation distance and the distribution becomes distinctly non-Gaussian. The red lines show the functions fitted to the distributions.